



Room-temperature-processed transparent hemispherical optoelectronic array for electronic eyes

Zhan Gao ^{#,a}, Liang Mei ^{#,b}, Jingkun Zhou ^{#,a,c}, Yang Fu ^h, Li Zhai ^{d,e}, Zhiyuan Li ^a, Ruijie Yang ^b, Dengfeng Li ^{a,c}, Qiang Zhang ^a, Jiahui He ^a, Jian Li ^{a,c}, Xingcan Huang ^a, Hu Li ^a, Yiming Liu ^a, Kuanming Yao ^a, Yuyu Gao ^a, Long Zheng ^g, Ye Chen ^g, Dangyuan Lei ^h, Hua Zhang ^{d,e,f,*}, Zhiyuan Zeng ^{b,f,*}, Xinge Yu ^{a,c,f,*}

Bio-inspired electronic eyes mimicking the geometry and function of natural light-sensing organs are highly attractive in next-generation miniaturized imaging systems. The processing of electronic eyes usually adopts complex and equipment-intensive techniques, involving vacuum-based materials growth, doping, deposition and patterning. Here, we report an electronic eye system with a fully transparent artificial retina by a simple solution-based method at room-temperature. The artificial retina contains a flexible 16×16 photodetector array, which composes of a ZnO nanoparticle-MoS₂ nanosheet composite film as the light sensing unit and the patterned silver nanowires as conductive paths within 1 cm². It shows a reliable ultra-violet response and high transparence across the visible and near-infrared range, and hence allows the artificial retina to perceive light from all directions without weakening the photo-response. Demonstrations of two kinds of electronic eye prototypes (concave and convex hemispheres) in a single device configuration show the possibility for double-sided imaging. This work provides a simple, rapid and high-throughput processing route for bio-inspired electronic eye that could be used for integration of various functional materials with different properties, which opens a new avenue for the multifunctional electronic eye devices.

Keywords: Electronic eye; Room-temperature processing; Curved electronics; MoS₂; Transparent photodetector array

Introduction

Biological eyes are remarkably exquisite organs that provide visual information for human and animals. Investigating diversified eye systems in nature, concave or convex curvature imagers unified with high density light-sensing units are the most typical ones. For instance, retina on the concave surface of the hemi-

^a Department of Biomedical Engineering, City University of Hong Kong, Hong Kong, China

^b Department of Materials Science and Engineering, and State Key Laboratory of Marine Pollution, City University of Hong Kong, Hong Kong, China

^cHong Kong Centre for Cerebro-Cardiovascular Health Engineering, Hong Kong, China

^d Department of Chemistry, City University of Hong Kong, Hong Kong, China

^e Hong Kong Branch of National Precious Metals Material Engineering Research Center, City University of Hong Kong, Hong Kong, China

^f Shenzhen Research Institute, City University of Hong Kong, Shenzhen 518057, China

⁹ Department of Chemistry, The Chinese University of Hong Kong, Hong Kong, China

^h Department of Materials Science and Engineering, City University of Hong Kong, Hong Kong, China

^{*} Corresponding authors.

E-mail addresses: Zhang, H. (Hua.Zhang@cityu.edu.hk), Zeng, Z. (zhiyzeng@cityu.edu.hk), Yu, X. (xingeyu@cityu.edu.hk).

^{*} These authors contributed equally to this work.

spherical human eyes enables high resolution and low optical aberration imaging characteristics [1,2]. Meanwhile, the convex structure in the compound eyes of arthropods offers exceptionally wide fields of view and high motion sensitivity [3,4]. Compared to conventional cameras with bulky setups, the hemispherical natural eyes adopt simple and compact optical configurations [5–7]. Therefore, bio-inspired electronic eyes mimicking natural light-sensing organs are promising for next-generation imaging systems and provide unique imaging characteristics for applications in a wide range of emerging fields beyond the existing technologies [6–8].

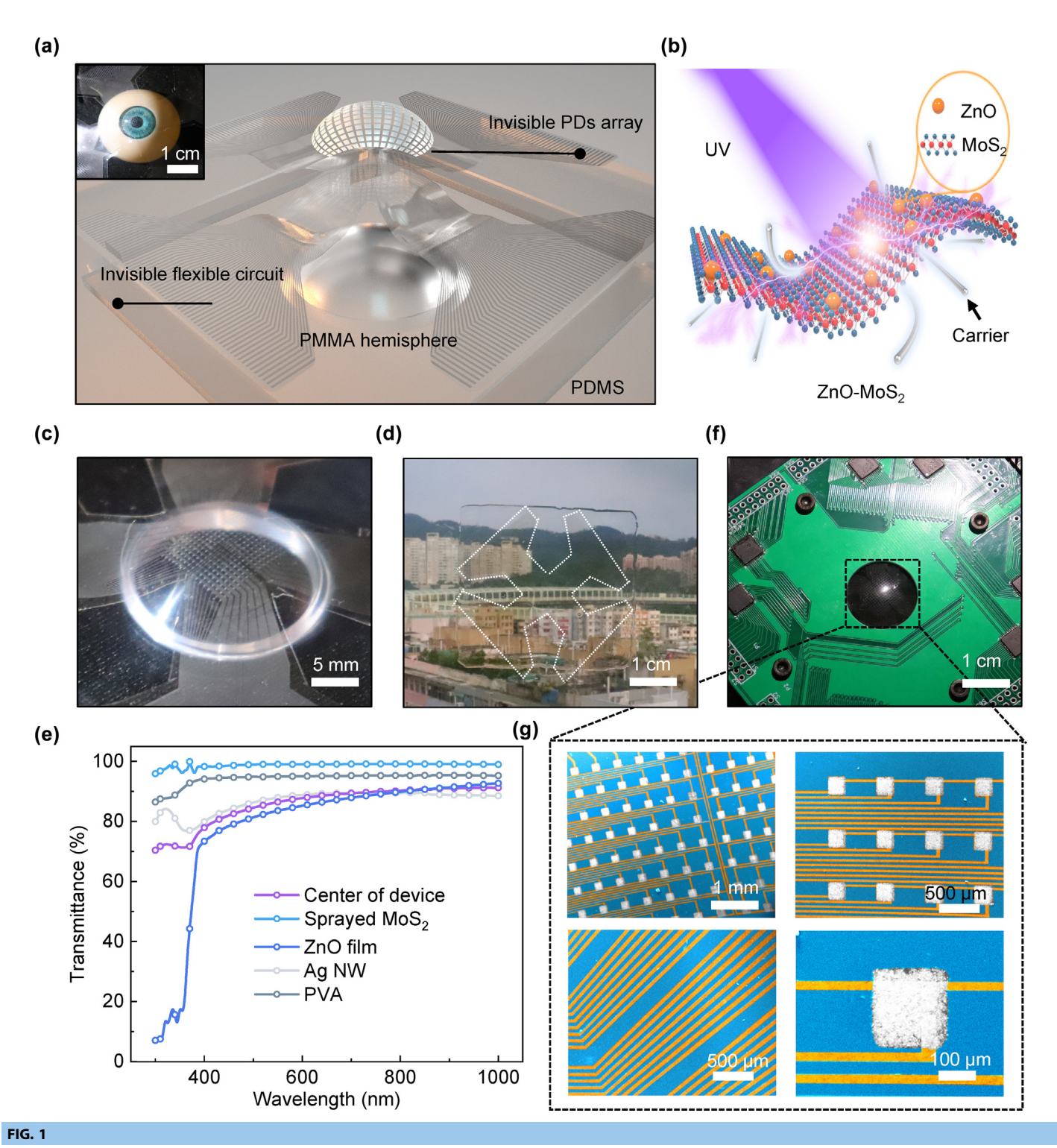
Since the development of bio-inspired electronic eyes and other biomimetic devices, design and fabrication of hemispherical configurations remains a great challenge for most [1,3,5,9-14]. Well-established fabrication technologies in semiconductor industries are exclusively for rigid planar surfaces, and hence incompatible for such configurations. At present, the most common method for fabricating hemisphere-shaped devices is to construct a sensing array of micrometer-scale photodiodes, such as Si nanomembranes, with mechanics designed interconnects on a soft planar surface, and then directly mount onto a hemispherical surface [3,5,10,11]. Island-bridge structured photodiodes with compressible interconnects can absorb the mechanical strain on the hemispherical surface to ensure the stable device performance [3,5]. Origami designs could also be used to enhance geometrical freedom and fill factor of photodiode arrays [10,11]. Besides silicon, emerging materials with excellent optoelectrical properties such as perovskite semiconductors also show great potential in biomimetic eyes [1]. However, extreme processing routes requiring high temperature and vacuum conditions significantly limit the applications in many aspects [1,3,5,9,11]. Therefore, there is a high demand to develop a high-throughput fabrication method suitable for a wide range of novel materials, ultimately making multifunctional electronic eyes with higher-level integration capacity.

Here, we report the room temperature, all-solutionprocessed fabrication of a bio-inspired electronic eye system, which employs a zinc oxide (ZnO)-molybdenum disulfide (MoS₂) photo-sensing array as a transparent retina. Patterned Ag nanowires (Ag NWs) embedded in an ultrathin Poly (vinyl alcohol) (PVA) film serve as transparent flexible electrodes and interconnects, while 16×16 thin-film junction devices of a ZnO nanoparticle (NP)-MoS2 nanosheet composite, referred to as ZnO-MoS₂, serve as optoelectronic sensing units. The processing routes and intrinsic flexibility of the materials enable directly mounting the photodetector array onto a hemispherical surface for fast ultra-violet (UV) detection in a robust manner. Furthermore, the remarkable optical transparency of the entire system (over 85% across the wavelength range of 450-1000 nm allows the artificial retina to perceive light from all directions without weakening its UV photo-response. Based on this feature, we demonstrate two kinds of electronic eye prototypes (concave and convex hemisphere) in one device configuration for double-sided imaging. These results open up the possibility of integrating energy harvesting modules such as solar cells for self-power, miniaturized and portable electronic eye systems.

Results and discussion

Fig. 1a shows the schematic illustrations of the electronic eye system with all-transparent optoelectronic components in an exploded view, and inset image shows the soft transparent electronic eye attached onto an eye model. The electronic eye system adopts a very simple structure, that associates with polymethyl methacrylate (PMMA) as the hemispherical substrate, transparent conducting Ag NWs as soft electrodes and interconnects, 16×16 thin-film photodetectors as the light sensing array, silicone polydimethylsiloxane (PDMS) as anchor pads, and a customized printed circuit board (PCB) (Supplementary Fig. 1). When the screws were tightened, PDMS (~0.8 mm) could be slightly squeezed to make sure the Ag NW pads well connected with protuberant pads on the PCB. The entire system closely mimics human eyes, where the incoming light beams can be focused on the artificial retina (photodetector array) by the hemispherical "eyeball" to generate optic nerve signals to the "brain" (Supplementary Fig. 2). The PMMA hemispherical dome with a radius of 15 mm imitate the shell of an eyeball, while the photodetector array on a soft and transparent PVA substrate can perfectly attaching on the "eyeball" to mimic the retina. Fig. 1b shows the schematic illustration of the ZnO-MoS₂ compositebased photodetector sensing unit for UV light optoelectronic response. ZnO NPs can be easily processed into thin film by spray-coating at room temperature and maintain its UVresponse under mechanical deformation [15-17]. Combined with inherently soft MoS₂ nanosheet, photo-generated charge carriers can be quickly separated by the built-in electrical field of the heterojunctions between ZnO-MoS₂, thus improving optoelectronic behaviors of the device. Fig. 1c shows the optical image of the electronic eye system, where it can be seen the soft photodetector array and Ag NWs circuit conformably interface with the hemispherical PMMA without any wrinkles. Spraycoating of Ag NWs and transfer printing technologies enable Ag NWs embedded in the PVA to form smooth, robust, and transparent electrical circuits [18-20]. The detailed fabrication process can be found in the Experimental section and Supplementary Fig. 3. The width of the conductive paths of the Ag NWs ranges from 30 μm to 250 $\mu m,$ serving as interconnects and connection pads to the data acquisition system (Supplementary Fig. 4a and b). As shown in Supplementary Fig. 5, we investigated the surface profile of the patterned Ag NWs embedded in PVA and the exposed Ag NWs on glass substrate. The embedded Ag NWs paths show smooth surface with a much lower Ra- \sim 15 nm while the exposed Ag NWs show rough surface with a $R_a \sim 182$ nm. Thus, by our fabrication process, no short circuits would be caused because of the roughness issues.

Since all the functional materials used in the electronic eye system are optically transparent, the device is "invisible" when attaching on the surface of other objects [21]. For instance, an optical image of the corresponding electronic eye attaching to the window exhibits remarkable transparency (Fig. 1d). The optical transmittance of different layers in the device are summarized in Fig. 1e, where the individual layers of MoS₂, ZnO, Ag NW and PVA all exhibit excellent transparency greater than 85 % between 450 nm and 1000 nm. As a result, the entire device with all these functional layers assembled yields an average transmit-



Bio-inspired electronic eye based on an all-solution-processed transparent retina. a, Schematic illustration of the electronic eye based on a fully transparent retina. Inset shows the transparent retina attached on an eyeball model. **b,** Schematic illustration of the light-sensing unit based on a ZnO NP-MoS₂ nanosheet composite. **c, d,** Optical images of the transparent retina mounting on the hemisphere dome and window. **e,** Optical transmission spectra of the transparent retina. **f,** Top-viewed optical image of our electronic eye system. **g,** Enlarged SEM image of the transparent photodetector array.

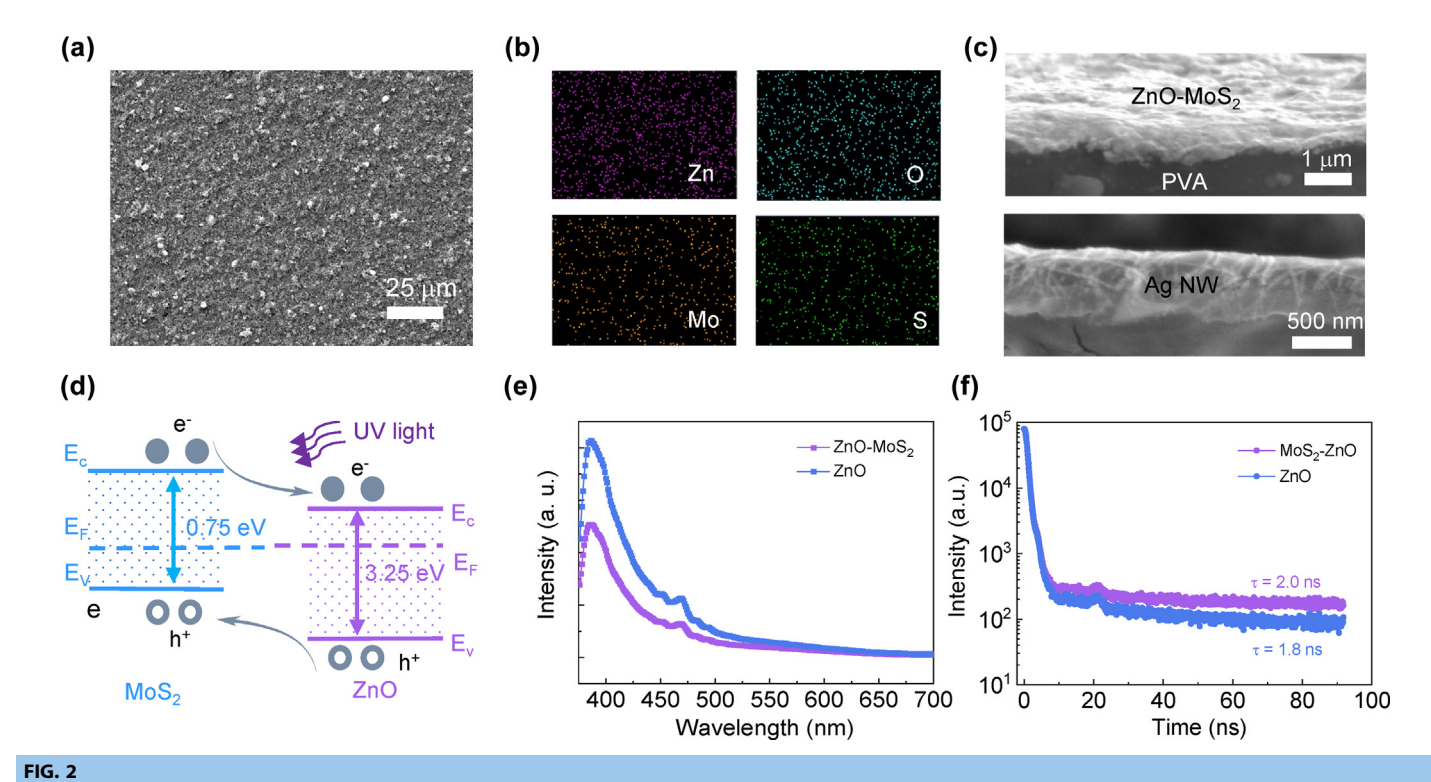
tance of $\sim\!85\%$ in the visible light range. The great transparency allows the photodetector array to response to the UV light from both front and back side without causing visible light intensity weakening. Fig. 1f shows the top view of the entire electronic eye system, where the soft photodetector array is attached on the curved PMMA surface, and the PCB connects to a semicon-

ductor analyzer for data acquisition. Enlarged views of the transparent photodetector array are shown in Fig. 1g and Supplementary Fig. 4c. The photodetector array is composed of 256 (16 \times 16) independent photodetector units within 1 cm² area and flexible circuit based on Ag NWs. The side length of each photodetector is 200 μm and the spacing between each

photodetector is 670 μm . The island structure of the photodetector array and the ultra-thin feature (450 nm) of each sensing unit ensure good mechanical properties. The Ag NW connection pads are aligned and connected with the protuberant pads on the PCB for electrical signal measurement.

The optoelectronic performance of the light-sensing units plays crucial roles in image acquisition for the electronic eye system. Here, MoS₂ nanosheets compositing with ZnO NPs form junctions allowing to improve the optoelectronic performance, in which MoS₂ nanosheets are used to enhance the separation/transport of photogenerated carriers [12,22]. The single-layer MoS₂ nanosheets are synthesized by our previously reported electrochemical lithium intercalation and exfoliation method [23-26]. The room temperature processing route enables high yield of the single-layer nanosheets as well as large-scale production [27]. Compared to bulk or multi-layered MoS₂, the MoS₂ nanosheet has the advantage of high transparency (Fig. 1e), which is essential in our device setup. Moreover, due to the difference with bulk or multi-layered MoS2 in quantum confinement effects and interlayer coupling, monolayer MoS2 exhibits higher carrier mobility and lower resistance, which can offer better performance in electronic devices. In contrast, multilayer MoS₂ suffers from interlayer interactions and coupling effects, resulting in more interference and scattering of carrier migration [28,29]. Atomic force microscopy (AFM) image and thickness statistical results of the exfoliated MoS_2 nanosheets show that 90 % nanosheets are single-layer (Supplementary Fig. 6a and b), which guarantees great transparency and excellent charge carrier transportation properties. Diffraction pattern showed the inner six

spots assigned to the (100) plane and outer six spots attributed to the (110) plane of the MoS₂ structure indicates good crystallinity of the exfoliated MoS₂ nanosheets (Supplementary Fig. 6c). As shown in Supplementary Fig. 7, the pure ZnO NPs also exhibits uniform nanoparticle morphology. Fig. 2a and Supplementary Fig. 8 show the top-viewed scanning electron microscopy (SEM) images and surface profile image of the ZnO-MoS₂ composite channel of the photo sensing unit. The ZnO-MoS₂ composite channel shows uniform morphology, which can ensure reliable optoelectronic performance. The energy dispersive X-ray spectroscopy (EDS) mapping in Fig. 2b also shows uniform distribution of Zn, O, Mo, S, elements over the ZnO-MoS₂ composite channel. In Supplementary Fig. 9, we investigated detailed morphology of ZnO-MoS₂ composites under higherresolution. As exhibited in the TEM images (Supplementary Fig. 9a), ZnO NPs cover the smooth surface of MoS₂ nanosheets, the corresponding diffraction pattern show the (100) and (110) planes of MoS₂ structure, and the (100), (002), (102), (103) and (110) planes of ZnO are also clearly presented in Supplementary Fig. 9b and c. Supplementary Fig. 9 d displays the HRTEM image of ZnO-MoS₂ composites, the measured lattice space of 0.270 nm assigned to the (100) plane of MoS2, as well as 0.280 nm and 0.248 nm attributed to the (100) and (101) plane of ZnO are well consistent with the theoretical values, respectively. HAADF-STEM images (Supplementary Fig. 9e-i) demonstrate the existence of Mo, S, Zn, O elements in the sample. From these TEM images, we can tell that ZnO nanoparticles are connected with MoS₂ nanosheet by tight and thorough physical contact and remain their nanostructures. As shown in cross-sectional



Structural and optical properties of the ZnO-MoS₂ composite. a, b, SEM image of a ZnO-MoS₂ composite (a) and corresponding EDS mapping (b). c, Cross-sectional images of the ZnO-MoS₂ composite. d, Schematic illustration of the UV-photodetection mechanism of the ZnO-MoS₂ composite. e, TRPL decay spectra of ZnO-MoS₂ and ZnO samples. The excitation source is a 365 nm picosecond laser. f, PL spectra of ZnO-MoS₂ and ZnO thin films ($\lambda_{\rm exc}$ = 365 nm).

SEM images (Fig. 2c), the ultrathin thickness and natural softness of the device could decrease the bending induced strain, ensuring stable optoelectronic performance in curved system [12]. From XRD spectrum of ZnO in the ZnO-MoS₂ composite (Supplementary Fig. 10a), featured peaks are well indexed to (100), (002), (101), (102) and (110) crystal planes of hexagonal ZnO structure (JCPDS no 36–1451). Raman spectrum (Supplementary Fig. 10b) of exfoliated MoS₂ nanosheets in the ZnO-MoS₂ composite shows the J₁ J₂ J₃ peaks at 153 cm⁻¹, 233 cm⁻¹ and 325 cm⁻¹ and two shoulder peaks at 380 cm⁻¹ (E_{2g}) and 405 cm⁻¹ (A_{1g}) [30,31], indicating both 1 T and 2H MoS₂ prepared here [32,33]. Moreover, as shown in Supplementary Fig. 11, the Mo_{3d} and S_{2p} spectrums of exfoliated MoS₂ nanosheets prove that both the 2H and 1 T MoS₂ structure fabricated [26], in agreement with Raman result. Two dominated peaks at 98 cm⁻¹ and 438 cm⁻¹ are observed in Raman spectrum of ZnO, ascribing to E2 (low) and E2 (high) mode of ZnO structure, indicating that the sample has great crystal quality [34]. The high electrical conductivity of 1 T MoS₂ within our synthesized nanosheets could also contribute to photo-generated charge transport of the photo sensing unit under illumination [35–37]. So far, these results confirm the high-quality crystallization of the ZnO-MoS₂ structure, which is essential to reduce charge traps and facilitate charge separation\transport, thus advantageous for optoelectronic performance [38,39].

UV–Visual absorption spectrum was used to investigate the bandgap of ZnO and MoS_2 , which can be calculated through the following equation (1):

$$(\alpha h v)^{\frac{1}{n}} = A(h v - E_{\varphi}) \tag{1}$$

Where α is absorption coefficient, A is a constant, h is the Planck constant, v is the frequency of the incident light, E_g is bandgap energy, and n is equal to 1/2 for ZnO and MoS₂ (direct transition) [40]. UV-Visual absorption spectrum and corresponding Kubelka-Munk transformed reflectance spectra of ZnO and MoS₂ are displayed in Supplementary Fig. 12, the bandgaps of ZnO and MoS₂ are calculated to be 3.25 eV and 0.75 eV. Our synthesized MoS₂ via the lithium intercalation-based method contains both 1 T and 2H phases [41]. Therefore, our synthesized MoS₂ nanosheets show smaller bandgap than the pure singlelayer 2H MoS₂ nanosheet (1.8 eV) and n-type behaviors because of the existing 2H MoS₂ nanosheet [32,42–44]. The work functions of the ZnO nanoparticles and MoS2 nanosheets are measured by ultraviolet photoelectron spectroscopy spectrum (UPS), which are calculated as 5.9 eV and 3.0 eV (Supplementary Fig. 12e and f). The energy band diagrams are shown in Fig. 2d. The difference in work functions of ZnO NPs and MoS₂ nanosheets could cause electrons diffusion at the junctions to balance the Fermi level [45,46]. As a result, n-n heterojunctions are formed between n-ZnO NPs and the n-MoS₂ nanosheets, resulting in improved charge separation\transport ability. When UV light illuminating the device, photo-generated carriers can be quickly separated by the built-in electrical field and transferred to electrodes under voltage bias, and thus resulting in improved optoelectronic performance [45-49]. Moreover, the 1 T MoS₂ within our synthesized MoS2 nanosheets could also facilitate carrier transport under illumination. To investigate the charge transfer and separation efficiency in ZnO-MoS₂ composite, photoluminescence spectrum (PL) and time-resolved photoluminescence spectrum (TRPL) spectrum were measured. PL spectrum presented in Fig. 2e shows that an emission peak at 386 nm appears after exciting at 365 nm. It is obvious that the peak intensity of the composite quenched a lot after loading MoS₂, ascribing to the fast electron transfer within ZnO nanoparticle-MoS₂ nanosheet composite film, which can suppress the recombination of electrons and holes. Fig. 2f shows the TRPL result of the ZnO and ZnO-MoS₂ composite under excitation at 365 nm. The TRPL decay spectrum curves were fitted by an exponential decay kinetics function expressed as the following equation (2).

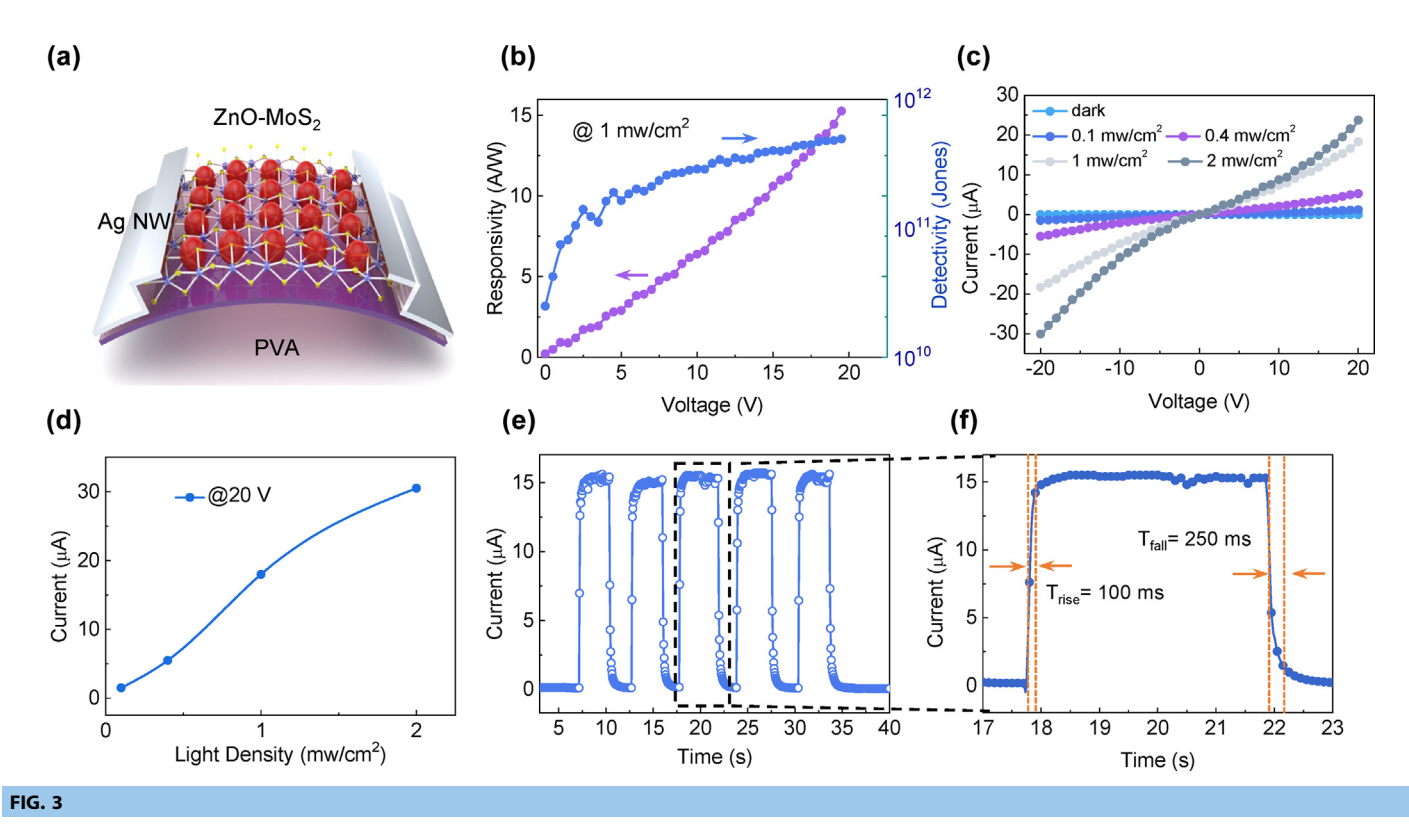
$$I(t) = A_1 \times e^{-\frac{t}{\tau_1}} + A_2 \times e^{-\frac{t}{\tau_2}} \tag{2}$$

Meanwhile, the average emission lifetime (τ) , reflecting the overall emission decay behavior, was calculated through below equation (3):

$$\tau = \frac{A_1 \tau_1^2 + A_2 \tau_2^2}{A_1 \tau_1 + A_2 \tau_2} \tag{3}$$

The charge carrier lifetime of $ZnO-MoS_2$ composites (2.0 ns) is higher than that of the pure ZnO (1.8 ns), indicating that ultrathin MoS_2 nanosheets enhance the separation efficiency of electrons and holes [22,50]. Such results are also consistent with the PL results, indicating excellent charge transfer and separation efficiency in $ZnO-MoS_2$ composite.

Fig. 3a shows the schematic diagrams of a single photodetector unit based on ZnO-MoS₂ nanosheet composite. As the UV light illuminates on the photodetector array, the illuminated sensing pixels in the electronic eye would produce photo current. Thus, the current on/off ratio of the photodetectors is the key parameter. Compared to other transition metal dichalcogenide nanosheets (WS2 and TaS2 nanosheets) fabricated by our developed fabrication process [25], MoS₂ nanosheets have prominent effect on the photo-response of the devices. WS2 nanosheets and MoS₂ nanosheets have similar atomic structure and exhibit similar material properties. As a result, the devices with WS₂ nanosheets devices show similar but less powerful photo-response behavior compared to the devices with MoS₂ nanosheets, as seen in their photo response curves (Supplementary Fig. 13 a and b). TaS₂ nanosheets by our fabrication process only have metallic properties [51,52] so the devices with TaS₂ nanosheets show more linear photo-response curves and higher dark current, resulting in lower on/off ratio. We also compared the stability of the devices under air-condition. The devices with MoS₂ nanosheets and WS₂ nanosheets are stable under airconditions while the devices with TaS2 nanosheets shows poorer air stability due to the instability of TaS₂ nanosheets in the presence of air, making them prone to oxidation [53]. To find the optimized performance of the sensing unit, we then investigated the device performance of the ZnO-MoS₂ photodetectors with different concentrations of ZnO NPs. The film thickness of the sensing layer is associated with ZnO NPs concentration, where higher concentration results in thicker film (Supplementary Fig. 14). As shown in Supplementary Fig. 15a and b, the device with 3 wt% ZnO NPs exhibits a photo responsivity of 3.2 A/W at a bias of 5 V. When the concentration of ZnO NPs increases to 4 wt%, the photo responsivity increases to 3.7 A/W at a bias of 5 V. However, further increasing ZnO NPs concentration to



Device performance measurements of ZnO-MoS₂ composite based photodetectors. a, Schematic illustration of a single pixel based on the ZnO NP-MoS₂ nanosheet composite. **b,** Responsivity and detectivity of the photodetector under 1 mw/cm² illumination. **c,** I-V curves of the photodetector under 365 nm light illumination with varied intensity and **d,** the photocurrent as a function 365 nm light intensity extracted from **c. e, f,** Dynamic photo-response measurements of the photodetector under 1 mW/cm².

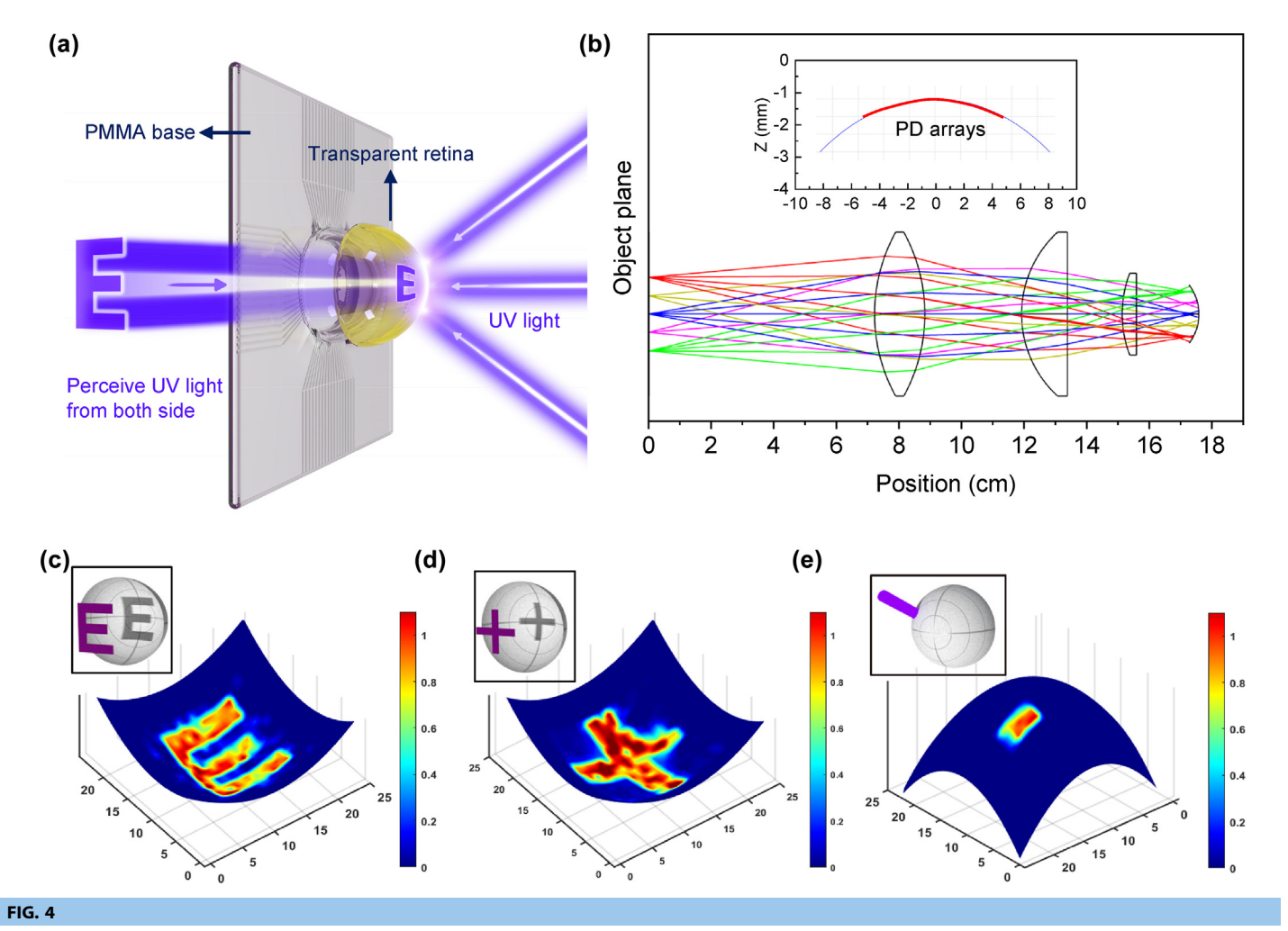
5 wt% and 6 wt% causes a decrease in photo responsivity, 2.37 A/ W and 1.2 A/W respectively. Supplementary Fig. 15c shows that the dark current of the device increases gradually from 3.2nA to 10.8nA with increasing concentration of ZnO NPs from 3 wt% to 6 wt%. In addition, the film thickness could be further increased by increasing spray duration. Extension the spray duration by 3 times with all the other parameters unchanged leads to a significant deterioration of dark current, where the device with 6 wt% ZnO NPs plus 3 times longer spray duration shows a dark current of 1.01 μA, which is 3 orders of magnitudes higher that of the normal device with 6 wt% ZnO NPs. Such an increase of dark current could be attributed to denser film that results in larger number of ZnO neighboring particles. Meanwhile, absorption of oxygen could be limited deep in the dense film and lead to ZnO domains that are less electron-depleted, thus higher film conductivity. Moreover, such ZnO domains are also less lightsensitive which decrease the number of photo-generated carriers leading to decrease of photocurrent [54]. So, film thickness is critical to the device performance. With an optimized concentration of 4 wt%, the devices show highest on/off ratio over 10³ under 5 V (Supplementary Fig. 15d), which is much higher than the conventional silicon photodector [1,3,11]. Thus, we choose the optimized concentration of 4 wt% ZnO NPs to fabricate the electronic eye device to get the best image results. Then the detailed performance of the devices with 4 wt% ZnO NPs as the optimized parameter are further investigated. As shown in Fig. 3b, the devices with 4 wt% ZnO NPs show a high detectivity over 10¹¹ Jones and a high responsivity of 15.2 A/W under a bias of

20 V. Fig. 3c and 3d show the photocurrent under different light intensity from 0.1 mw/cm² to 2 mw/cm². Under illumination of 365 nm light, the devices can generate an approximately linear response to different light intensities, confirming the sensitive response of the devices. The dynamic photo response measurements under 1 mw/cm² illumination are shown in Fig. 3e and f. The device shows fast and repeatable photo response, indicating excellent stability and reproducibility under multiple cycles of illumination. The response and recovery time of the device of 4 wt% ZnO NP-MoS₂ are 100 ms and 250 ms, respectively, which are much faster than pure ZnO NPs photodetectors [55-59]. The fast response time in the ZnO NP-MoS₂ photodetectors associates with the unique carrier transport behaviors between heterojunction of ZnO NPs and MoS2 nanosheets mentioned above. Such rapid light response can easily meet the highspeed data acquisition requirements of electronic eye systems. Then the photocurrents of the devices under bending condition are measured (Supplementary Fig. 16). Owing to intrinsic flexibility of the sensing layer, the device shows very stable lightresponse under various bending condition. Such stable mechanical property ensures the function of the photodetector array even mounting on a curvy surface.

After testing the performance of individual pixel devices, we investigated the imaging characteristics of the transparent photodetector array mounting on the curvy surface. The fabricated free-standing soft photodetector array needs to be mounted on the surface of the customized PMMA dome (Supplementary Fig. 17), anchored with PCB by PDMS pad between the PCB

and PMMA substrate. As shown in Supplementary Fig. 4, aligned and tightened contact between pads on PCB and flexible circuit ensure stable connections for data acquisition. Supplementary Figs. 18–20 present the PCB layouts and mechanism of data acquisition for the electronic eye system [60]. As shown in Supplementary Fig. 21, we tested the transfer characteristic curves for all the pixels. The photo current distribution of all the pixels (under a bias of 5 V and 0.4 mw/cm² light intensity) shows good uniformity, which is owing to the optimized processing procedures of the spray-coating technology, and thus allow the array to exhibit uniform electrical properties for good imaging quality. The scanning circuit consists of a control board (Arduino nano) and eight pieces of 32-channel multiplexer. Arduino nano controls the multiplexers to turn on the selected channel and close the other channels. A semiconductor analyzer is connected to the positive and negative ends of the conductive channels, and the signal from the corresponding pixel can be measured and collected [61]. The control board automatically sweeps the activated channel under the frequency of 1 Hz, and thus the data from all the photodetectors can be collected and traversed to obtain the image.

In general, most biological eyes in nature have simple compound or chambered structures with unique optical imaging properties. The current reported bio-inspired electronic eye systems usually mimic either of the two structures as an imager. Fig. 4a shows the schematic illustration of the electronic eye imaging system. The optical transparency of the artificial retina allows the electronic eye system to perceive light from both front and back sides (Supplementary Fig. 22). This is due to the high light transmittance of the PVA substrate, which exceeds 93% at 365 nm (Fig. 1e). As a result, the photodetector can effectively respond to UV light by both concave and convex configurations, and thus to realize two kinds of natural eye prototypes (concave and convex hemisphere) in one device configuration. For mimicking the chambered eve with concave hemisphere, the light passes through a simple lens set-up (Supplementary Fig. 23 and Table 1) and focuses on the concave side of the artificial retina. Compared to conventional flat imagers with bulky lens elements or corrective optics, the concave imager could adapt its photo sensing area into curve surface to match the field curvature and offers several advantages, including a wide field of view, low optical aberration, and a simplified optical setup (Supplementary



Demonstrations of the Double-sided imaging. a, Schematic illustration of our transparent retina perceiving UV light from all directions. **b,** Ray-tracing simulation of the lens set-up. Inset shows well matched curvature of photodetector array with the focal plane. **c, d,** Reconstructed images of letter "E" and symbol "+" captured by a chambered electronic eye prototype. **e,** Reconstructed image of "·" captured by a compound electronic eye prototype. The numbers 0–25 represent plane space location of the sensing units. The color bar represents the greyscale values.

Fig. 24) [1,5,7]. Fig. 4b presents the simulated ray trace of the lens set-up. The hemisphere focal plane is simulated as a curvy surface with a radius of 15 mm which is well matched with the curvature of the soft photodetector array (Fig. 4b inset and Supplementary Fig. 24). Controlled by the Arduino nano chip, the photo current of each photodetector can be collected and optimized, and then for image reconstruction. The values of the photo current in the corresponding sensing pixels are then converted into greyscale values and enumerated in a 16 by 16 matrix. Specifically, the greyscale values between 0 and 1 are calculated by the equation (4) as followed,

$$Grey = \frac{I_{light} - I_{dark}}{I_{full} - I_{dark}} \tag{4}$$

where Grey is the greyscale value, I_{light} , I_{full} and I_{dark} are the recorded current values of the devices under specific illumination, full light illumination and dark conditions. Then the pixelated image (Supplementary Fig. 25) was optimized by applying the interpolation function of MATLAB (Supplementary Note 1). Fig. 4c and d show the mimic human eye imaging capabilities of the electronic eye system associates with imaging patterns of a letter 'E' and a cross shape in the front side. Furthermore, without changing device architecture and connection set ups, the electronic eye system can also simulate the function of insect compound eyes by imaging from the back side. As shown in Fig. 4e, the electronic eye can also capture the light from the convex side by the photodetector array. For the convex imager, it could have a wide field of view and nearly infinite depth of field. The same pattern letter used in the concave configuration could be used to illuminate the convex side and rise the photocurrent, but the image quality would not be good enough because of the optical aberration. Herein, a 365 nm laser diode was employed to illuminate upon the convex side of photodetector array from an angle of ${\sim}45^{\circ}$ and the current of the corresponding photodetectors increase obviously, while the other unilluminated photodetectors remain in their dark states. By integrating these two configurations into on single device setup, we propose a novel concept of multifunctional electronic eyes, leveraging the high transparency of our device. This approach aims to enhance the system-level integration capacity of electronic eye system. Moreover, such imaging function can be further improved to obtain a wide-angle field of view or high motion sensitivity by applying micro-lens on each pixel [3]. The potential of integrating transparent soft photodetector array with solar cell devices to realize self-powered electronic eye system has been demonstrated in this work. UV electronic eye system could have wide potential realworld applications in the field of safety and protection. They can be used for flame detection, monitoring of chemical leaks and measurement of radiation dose, providing an effective means of industrial safety and personal protection. These applications need long term and continuous operation of the UV sensors, so concept of self-powered UV electronic eye could be very useful. As shown in Supplementary Figs. 26a and b, the soft photodetector array is attached on the surface of a commercial flexible solar cell array. Due to the high optical transparency of the photodetector array, majority of the visible light can penetrate the artificial retina and be absorbed by the solar cells. The voltage generated by the solar cells at back of the artificial retina only show slight

reduction that of solar cells directly illustrated by light. Thus, the self-powering feature shows the potential for providing voltage bias to the photodetector array without additional wired power supplies (Supplementary Fig. 26c), which can significantly improve the portability of the electronic eye system.

Conclusion

In conclusion, we have developed an electronic eye system with a transparent hemispherical retina by all solution process at room temperature. Detailed material selection, mechanical design and system-level integration proved the excellent performance, robust operation behaviors, and high throughput processing methods of the transparent artificial retina. Such unique transparence allows the retina to perceive light from all directions without weakening of the photo-response. Furthermore, two kinds of electronic eye prototypes (concave and convex hemisphere) in one device configuration for double-sided imaging have been demonstrated. This work offers a new opportunity from materials, mechanics and processing routes for bioinspired electronic eye.

Methods

Materials. Molybdenum disulfide powder (MoS₂, Innochem), Tungsten disulfide (WS₂, Macklin), Tantalum disulfide (TaS₂, Sixcarbon technology), copper foil (Shenzhen Kejing Star Technology Company), lithium foil (DodoChem), 1 M LiPF₆ dissolved in a mixture of ethyl carbonate (EC), dimethyl carbonate (DMC) and ethyl methyl carbonate (EMC) at a volume ratio of 1:1:1 (DodoChem), polypropylene (pp) film (Celgard 2300, North Carolina, USA), poly(vinylidene fluoride) (PVDF, fluorochem), N-methylpyrrolidone (NMP, J&K Scientific Ltd), acetone (Macklin), deionized water was purified using Milli-Q System. Zinc Oxide nanoparticles, (Sigma-Aldrich, \leq 40 nm avg. part. size, 20 wt% in H₂O). Silver nanowire (XFNano, average length: 20 μm, diameter: 30 nm. 5 mg/mL dispersed in ethanol). Poly (vinyl alcohol) (Sigma, Mw 31000-50000, 98–99% hydrolyzed).

Preparation of single-layer MoS₂ nanosheets. Bulk MoS₂ was coated on the copper surface and assembled in lithium-ion battery used as cathode, lithium foil as anode and dissolved LiPF₆ as electrolyte. Lithium was driven into the interlayer of the bulk MoS₂ structure via performing galvanostatic discharge process, after finishing the intercalation via controlling the discharging condition, the lithiated sample (Li_xMoS₂) was taken out from the battery and sonicated in DI water, then opaque suspensions were obtained, which was washed and purified for characterization and composited with ZnO. The preparation method for WS2 and TaS2 nanosheets is similar to that of MoS2 nanosheets but applied bulk WS2 and TaS2 coated copper foil as the cathode, respectively. Besides, there are variations in the discharge current and cutoff voltage during the galvanostatic discharge process. For MoS₂, the discharge current is 0.05 mA and the cutoff voltage is 0.9 V. For WS2, these values are 0.1 mA and 0.7 V respectively. As for TaS2, the discharge current is 0.025 mA with a cutoff voltage of 0.9 V.

Fabrication of ultraviolet photodetector based on ZnO NP-MoS₂ nanosheet composites. The glass substrates

were cleaned in an ultrasonic bath with detergent water, acetone, deionized water, and isopropyl alcohol for 15 min each sequentially. Then the substrate was treated with energetic oxygen plasma (45 W) in a Harrick plasma cleaner for 5 min to create a hydrophilic surface. Assisted by a metal mask with designed pattern, Ag NW solution was sprayed onto glass substrate with a discharge speed of 40 µL/30 s by an IWATA HP-CP spray gun (0.3 mm) connected with a portable air pump at an air pressure of 15 psi. Then two coplanar electrodes with 100 μm width were formed. Next, aqueous solution of PVA was drop-casted onto the glass substrate. Since the PVA solutions were drying naturally to form a thin and soft film, the thickness, softness and stickiness were controlled by the concentration of PVA solution and we found 10 wt% aqueous solution of PVA could result in the best thin film (\sim 20 μ m) when considering these parameters. After drying naturally at room-temperature, the PVA film embedded with coplanar electrodes was peeled off from the substrate, resulting in stable and smooth conductive surface. For the different two-dimensional transition metal dichalcogenides comparison experiment, the MoS₂, WS₂ and TaS₂ nanosheet dispersion were mixed with 4 wt% ZnO NP dispersion and stirred for 24 hrs. This concentration was defined by weight of ZnO NPs divided by whole solution weight. The mixed solution was well-dispersed by ultrasonication for 5 min before casting. Then using a metal mask, the mixed solution was sprayed onto the PVA film by a spay gun with at an air pressure of 25 psi generated by air pump for ~12 s and baked in 80 °C drying oven for 5 min to form patterned thin-film ultraviolet photodector. For the ZnO-MoS₂ thickness comparison, the ZnO NP dispersion was mixed with MoS₂ nanosheet dispersion directly with concentrations of 3-6 wt% and followed with same fabrication process. For the device with 6 wt% ZnO NPs with a thicker film, the spay duration is $\sim 30 \text{ s}.$

Fabrication of transparent photodetector array.

The fabrication of transparent photodector array was all based on solution process as described in Supplementary Fig. 3. It began with spray-coating Ag NW solution onto whole precleaned $7.5 \times 7.5 \text{ cm}^2$ glass substrate as the same spray-coating parameters described above. After deposition of Ag NW film, photolithography and developing defined a layer of patterned hard photoresist (PR, AZ 4620, AZ Electronic Materials) on the surface of Ag NW film. Then a sash style paint brush was used to remove the exposed Ag NWs, followed by immersion of the substrate in Acetone for 10 min to remove the photoresist, then desired pattern of Ag NW film was developed. The thinnest path and minimum separation of the Ag NW circuit was 30 µm. Next, 10 wt% aqueous solution of PVA was drop-casted onto the patterned Ag NW film. After drying naturally at roomtemperature, the PVA film embedded with patterned Ag NW circuit was peeled off from the substrate. Then a metal mask with designed pattern of square array was used to spray coating 4 wt % ZnO-MoS₂ solution onto PVA film as the same spray-coating parameters described above. Then surplus part of the PVA film was cut off by scissors, resulting in a cross shape. Finally, the free-standing soft photodector array was mounted on the designed PMMA dome, anchored with custom-made PCB by PDMS pad between the PCB and PMMA substrate. Aligned and

tighten contact between pads on PCB and flexible circuit ensured stable connection for image acquisition (Supplementary Fig. 4).

Material characterizations and photodetector **measurement.** The surface morphologies were measured using top-view scanning electron microscopy (SEM, FEI Quanta 450 FESEM) and atomic force microscope (Bruker Dimension Icon AFM). The electronic performance of photodetector unit was measured by Keysight B1500A Semiconductor Analyzer. Surface image of ZnO-MoS2 was characterized through AFM (Dimension 3100, Veeco, CA), TEM (FEI talosf200s) and SEM (FEI Quanta 450 FESEM). Raman shift was carried out on WITEC RAMAN alpha 300R, with a laser excitation wavelength of 532 nm and power of 1 mW. XRD was carried out on BRUKER SRD-D2 Phaser. PL spectrum and time-resolved PL decays were performed on floriba-fluoromax-4 and FLS920P spectrometer with excitation wavelength of 365 nm. Work function of MoS2 and ZnO was measured via UPS on ESCALAB 250 Xi. Chemical composition and surface states of exfoliated MoS2 were investigated by XPS (Thermo Scientific K-Alpha Nexsa).

Assembling of the electronic eye system. To precisely mount the retina on the eyeball, the soft PVA substrate was first attached to the PCB according to the designed loci, and the connection Ag NW pads embedded in the substrate were aligned and connected with the protuberant pads on the PCB. Then the photodetector array could be placed right in the center of the skeletonized circular hole on the PCB. Four soft PDMS anchor pads (~0.8 mm thick, 4 cm long, 5 mm wide) were attached on the positions of the protuberant pads on the PCB. Then the PMMA hemispherical dome then tightly lifts the soft photodetector array from below to avoid gaps. Finally, screws & nuts that run through the upper PCB and bottom PMMA substrate were tightened to stabilize whole system.

Double-sided image acquisition of electronic eye with transparent retina. The detailed setup of electronic eye system is shown in Supplementary Fig. 23. For chambered eye prototype, an ultraviolet light-emitting diode blocked by patterned mask provided patterned light, such as cross and letter 'E'. Through a simple lens setup, the passed light was focused on the concave side of photodetector array. For compound eye prototype, a 365 nm laser illuminated upon the convex side of photodetector from an angle of ~45°. For both concave and convex prototypes, the current of each photodetector was measured by Keysight B1500A Semiconductor Analyzer. The scanning circuit was composed of an Arduino nano and eight 32channel multiplexers. Keysight B1500A probes were connected to the channels, and the corresponding sensors could be measured, so that Arduino nano automatically switched the activated channel, all the sensors of the device could be traversed to obtain the image. Then the normalized signal was extracted from the data and reconstructed by the interpolation function of MATLAB.

Author contributions

Z.G., L.M. and J.Z. contributed equally to this work. Z.G. and X. Y. conceived the ideas and designed the experiments. Z.G., L.M., J.Z., H.Z., Z.Z. and X.Y. wrote the manuscript. Z.G., L.M., J.Z., Y. F., Z.L, R.Y., D.L., Q.Z., J.H., J.L, X.H., H.L., Y.L., K.Y., Y.G., L.Z.,

Y.C. and L.Z. performed experiments and analyzed the experimental data. Y.F. and D.L. performed optical transmission experiments. J.Z. performed the circuit design and software programming.

CRediT authorship contribution statement

Zhan Gao: Conceptualization, Methodology, Investigation, Data curation, Writing - original draft, Writing - review & editing. Liang Mei: Investigation, Data curation, Writing - original draft. Jingkun Zhou: Software, Investigation. Yang Fu: Investigation, Software. Li Zhai: Writing – review & editing. Zhiyuan Li: Investigation, Data curation. Ruijie Yang: Data curation. Dengfeng Li: Data curation, Writing - review & editing. Qiang Zhang: Investigation, Data curation. Jiahui He: Data curation. Jian Li: Data curation. Xingcan Huang: Data curation. Hu Li: Data curation. Yiming Liu: Data curation. Kuanming Yao: Data curation. Yuyu Gao: Data curation. Long Zheng: Investigation, Data curation. Ye Chen: Writing - review & editing. **Dangyuan Lei:** Writing - review & editing. Hua Zhang: Writing - review & editing, Project administration, Funding acquisition. Zhiyuan Zeng: Writing - review & editing, Project administration, Funding acquisition. Xinge Yu: Conceptualization, Methodology, Writing – review & editing, Supervision, Project administration, Funding acquisition.

Data availability

No data was used for the research described in the article.

Declaration of Competing Interest

The authors declare that they have no known competing financial interests or personal relationships that could have appeared to influence the work reported in this paper.

Acknowledgements

This work was supported by National Natural Science Foundation of China (Grants No. 62122002), The City University of Hong Kong (Grants No. 9610423, 9667221, 9680322, 9360165), partially supported by InnoHK Project on Project 2.2—AI-based 3D ultrasound imaging algorithm at the Hong Kong Centre for Cerebro-Cardiovascular Health Engineering (COCHE). Z.Y. Zeng thanks ECS scheme (CityU9048163) from RGC in Hong Kong and the Basic Research Project from Shenzhen Science and Technology Innovation Committee in Shenzhen, China (No. JCYJ20210324134012034). H.Z. thanks the support from the Science Technology and Innovation Commit-Municipality tee of Shenzhen (grant JCYJ20200109143412311), the Research Grants Council of Hong Kong (AoE/P-701/20), the Start-Up Grant (Project No. 9380100) and the grants (Project Nos. 9678272, 9680314, 7020013 and 1886921) from the City University of Hong Kong, and ITC via the Hong Kong Branch of National Precious Metals Material Engineering Research Center (NPMM).

Appendix A. Supplementary data

Supplementary data to this article can be found online at https://doi.org/10.1016/j.mattod.2023.08.004.

References

- [1] L. Gu et al., Nature 581 (2020) 278-282.
- [2] M.F. Land, Contemp. Phys. 29 (1988) 435.
- [3] Y.M. Song et al., Nature 497 (2013) 95-99.
- [4] J. Duparré et al., Appl. Opt. 44 (2005) 2949.
- [5] H.C. Ko et al., Nature 454 (2008) 748-753.
- [6] M.S. Kim et al., Adv. Mater. Technol. 2100144 (2021).
- [7] G.J. Lee et al., Adv. Funct. Mater. 28 (2018) 1705202.
- [8] F.Y. Liao et al., Nat. Electron. (2022).
- [9] M.S. Kim et al., Nat. Electron. 3 (2020) 546-553.
- [10] K. Zhang et al., Nat. Commun. 8 (2017) 1782.
- [11] Z. Rao et al., Nat. Electron. 4 (2021) 513-521.
- [12] C. Choi et al., Nat. Commun. 8 (2017) 1664.
- [13] Q.Y. He et al., Nat. Electron. 2 (2019) 13-14.
- [14] X.G. Yu et al., Nature 575 (2019) 473-479.
- [15] D. Liu et al., Nature Photon. 8 (2014) 133-138.
- [16] I. Jeon et al., J. Mater. Chem. A 2 (2014) 18754-18760.
- [17] S.K. Hau et al., Appl. Phys. Lett. 92 (2008) 253301.
- [18] Z. Gao et al., J. Mater. Chem. C 8 (2020) 15105.
- [19] D. Emilie et al., Adv. Funct. Mater. 30 (2020) 2001251.
- [20] P. Pattanasattayavong et al., Adv. Mater. 25 (2013) 1504-1509.
- [21] X.G. Yu et al., Adv. Mater. 27 (2015) 2390-2399X.
- [22] X. Gu et al., Adv. Energy Mater. 3 (2013) 1262-1268.
- [23] Z.Y. Zeng et al., Angew. Chem. Int. Ed. 50 (2011) 11093-11097.
- [24] Z.Y. Zeng et al., Angew. Chem. Int. Ed. 51 (2012) 9052-9056.
- [25] R. Yang et al., Nat. Protoc. 17 (2022) 358-377.
- [26] L. Mei et al., Chem. Commun. 57 (2021) 2879-2882.
- [27] W. Chen et al., Nat. Nanotechnol. (2021).
- [28] A. Singh et al., Phys. Rev. B 105 (2022) 165430.
- [29] M.D. Sial et al., Nat. Commun. 9 (2018) 1442.
- [30] K. Leng et al., ACS Nano 10 (2016) 9208-9215.
- [31] Y. Chen et al., Nat. Rev. Chem. 4 (2020) 243-256.
- [32] Q.Y. Zhang et al., J. Mater. Chem. A 8 (2020) 15417-15444.
- [33] Y. Park et al., Adv. Mater. 32 (2020) 2001889.
- [34] Y. Zhou et al., J. Mater. Chem. A 6 (2018) 10286-10296.
- [35] M. Acerce et al., Nat. Nanotechnol. 10 (2015) 313-318.
- [36] Z.C. Lai et al., Nat. Mater. 20 (2021) 1113-1120. [37] Y.F. Yu et al., Nat. Chem. 10 (2018) 638-643.
- [38] X.M. Li et al., Adv. Funct. Mater. 26 (2016) 5903-5912.
- [39] X. Liu et al., Nat. Commun. 5 (2014) 4007.
- [40] D.P. Norton et al., Mater. Today 7 (2004) 34-40.
- [41] X. Huang et al., Nat. Commun. 4 (2013) 1444.
- [42] Y. Fang et al., J. Am. Chem. Soc. 141 (2019) 790-793.
- [43] G. Eda et al., Nano Lett. 11 (2011) 5111-5116.
- [44] Q. Tang et al., Chem. Mater. 27 (2015) 3743-3748.
- [45] X. Chang et al., Sensors Actuat.: B. Chem. 317 (2020) 128208.
- [46] J. Zhang et al., ChemistrySelect 5 (2020) 3438-3444.
- [47] X. Xu et al., Sensors Actuat.: B. Chem. 333 (2021) 129616.
- [48] H.Q. Liu et al., Appl. Surface Sci. 580 (2022) 152222.
- [49] A.D. Muhammad et al., Sensors Actuat.: B. Chem. 310 (2020) 127810.
- [50] J.W. Liu et al., Adv. Funct. Mater. 23 (2013) 4941-4948.
- [51] J.J. Wu et al., J. Am. Chem. Soc. 140 (1) (2018) 493-498.
- [52] J. Peng et al., J. Am. Chem. Soc. 139 (26) (2017) 9019–9025.
- [53] A.K. Geim et al., Nature 499 (2013) 419-425.
- [54] N. Nasiri et al., Adv. Mater. 27 (2015) 4336-4343.
- [55] Y.Z. Jin et al., Nano Lett. 8 (2008) 6.
- [56] B. Liu et al., J. Mater. Chem. 22 (2012) 9379.
- [57] C.Y. Yan et al., Adv. Mater. 26 (2014) 943-950.
- [58] J.H. Jun et al., Ceram. Int. 35 (2009) 2797-2801.
- [59] L.Q. Qin et al., IEEE Electron Device Lett. 32 (2011) 1.
- [60] J.H. He et al., Nano Energy 81 (2021) 105590.
- [61] Y.M. Liu et al., Sci. Adv. 8 (2022) eabl6700.